Nano Research

Open Access

Research Article

Transparent strain-insensitive stretchable ionic temperature sensor with MXene enhanced performance

Lingyun Cao[1,§], Yao Zhou[1,§], Juan Wang[1,§], Zhiwei Zhang[2,§], Bin Cheng[1], Zhihong Chen[1], Jiageng Pan[1], Jiaxiang Chen[1], Jiangfeng He[1], Xiaoxiao Ma[1], Honglong Li[1], Guowei Yang[1], and Fang Yi[1] ✉

[1] *School of Materials Science and Engineering, Nanotechnology Research Center, State Key Laboratory of Optoelectronic Materials and Technologies, Guangdong Functional Biomaterials Engineering Technology Research Center, Sun Yat-sen University, Guangzhou 510275, China*

[2] *Beijing Institute of Nanoenergy and Nanosystems, Chinese Academy of Sciences, Beijing 101400, China*

§ *Lingyun Cao, Yao Zhou, Juan Wang, and Zhiwei Zhang contributed equally to this work.*

Cite this article: *Nano Research*, **2026**, *19*, 94908861. https://doi.org/10.26599/NR.2026.94908861

ABSTRACT: Temperature is a fundamental physical quantity. With the rapid development of stretchable electronics, transparent stretchable temperature sensors are in critical demand. However, performance retention under strain is a great challenge, and the influence of the electrode on the sensing performance is rarely reported. Here, a transparent strain-insensitive stretchable ionic temperature sensor is developed, whose sensing performance is enhanced through an electrode engineering strategy by inserting MXene between two Ag NWs layers. MXene largely increases the electrode's adhesion strength to the ionogel electrolyte, and hinders ion adsorption while, in the meantime, bonds with neutral ion pairs whose dissociation enhances with increasing temperatures. The strain-insensitive sensing performance is mainly ascribed to a crack counteraction mechanism, where the boosting effect of the expanding electrode area as strain enlarges is counteracted by the decline in conductive paths owing to widening cracks. This crack counteraction mechanism is quantitatively verified through theoretical simulation. The sensor is demonstrated for various applications, including smart prosthetic hands, motion tracking, and temperature monitoring of a deforming surface. This work could inspire new stretchable sensor designs and guide strain-insensitive stretchable electronics.

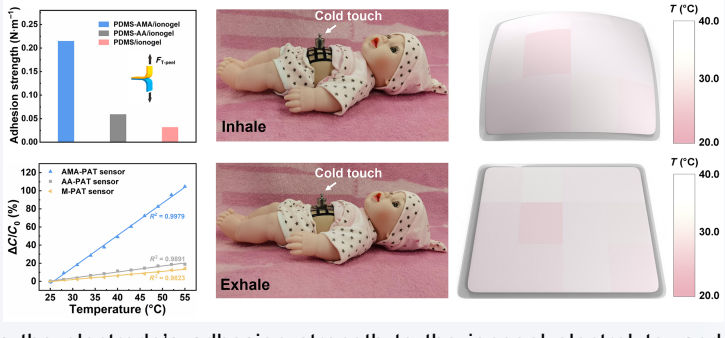

KEYWORDS: temperature sensor, strain-insensitive sensing, $Ti_3C_2T_x$ MXene, stretchable sensor

1 Introduction

Temperature is a fundamental physical quantity measured in daily, scientific, and industrial applications. With the fast development of stretchable electronics, which are recognized as next-generation electronics and expected to revolutionize various areas, stretchable temperature sensors with high transparency are in critical demand [1–5]. Transparent stretchable temperature sensors monitor temperature without obstructing the observation of the conditions of the monitored surface, which have significant applications in myriad areas such as medical care, electronic displays, prosthetics, and food testing [6–9]. Stretchable temperature sensors typically leverage the temperature dependence of electron, dipole, or ion motion within sensing materials to achieve their sensing function [10–16], categorizing mainly into resistive [17–19], thermoelectric [20, 21], pyroelectric [22, 23], and capacitive [24, 25] temperature sensing principles. Stretchable resistive temperature sensors detect temperature through resistance change, which have relatively simple device structures but often suffer from low reproducibility; stretchable thermoelectric temperature sensors detect temperature based on the thermoelectric effect, which work without external power source and have fast response time but cannot generate electrical outputs when there is no temperature gradient; stretchable pyroelectric temperature sensors detect temperature based on the pyroelectric effect, which have fast response to temperature fluctuation and are self-powered but cannot detect static

Received: March 22, 2026; **Revised:** April 26, 2026
Accepted: May 21, 2026

✉Address correspondence to yifang@mail.sysu.edu.cn

temperature. Stretchable capacitive temperature sensors detect temperature through capacitance change, which possess the advantages of drift-free operation, high sensitivity, and superior cyclic stability. In particular, with the rapid development of ionogels, stretchable temperature sensors employing the interfacial supercapacitive nature of ion adsorption/desorption emerge as an intriguing modality and attract increasing attention [26–30], which have the potential to satisfy the demand of high transparency along with high sensitivity and shape adaptability.

However, there have been few reports on stretchable temperature sensors achieving high transparency, and it is a great challenge to maintain the sensing performance under deformation. Furthermore, the relationship between the electric double-layer capacitance and temperature has been studied with an emphasis predominantly on the electrolyte, lacking examination with regard to the impact of the electrode on the sensing performance.

In this work, a transparent stretchable ionic temperature sensor is developed with strain-insensitive sensing performance, whose sensitivity is enhanced via an electrode engineering strategy through introducing MXene into two layers of silver nanowires (Ag NWs). The addition of MXene notably enlarges the adhesion strength of the electrode to the ionogel electrolyte, and suppresses the ion adsorption on the electrode surface, but meanwhile binds neutral ion pairs whose dissociation enhances with increasing temperatures, leading to more free ions on the electrode surface as temperature rises. The strain-insensitive sensing performance can be mainly ascribed to a crack counteraction mechanism that the reduced electron paths resulting from the widening cracks offset the promoting effect of the enlarging electrode surface area on the capacitance as the strain increases. This crack counteraction mechanism is quantitatively verified via theoretical simulation. The ionic temperature sensor can accurately detect the skin temperature despite various motions. A temperature alarm system was constructed based on the sensor, which can protect the prosthetic hand from cold/hot water by automatically triggering alarms. The ionic temperature sensor array can conveniently deliver the temperature distribution from handshaking between a prosthetic hand and a person, track the motion path of an electric warm worm, and monitor the temperature of a deforming doll's belly during breathing.

2 Results and discussion

2.1 Design and basic characteristics of the Ag NWs/$T_3C_2T_x$ MXene/Ag NWs (AMA)-PAT ionic temperature sensor

The transparent strain-insensitive stretchable ionic temperature sensor is structured with a poly(acrylamide-co-trifluoroethyl acrylate) (P(AAm-co-TFEA))/ionic liquid 1-ethyl-3-methylimidazolium bis(trifluoromethylsulfonyl) imide ([EMIM][TFSI]) (PAT ionogel) electrolyte sandwiched between two designed stretchable electrodes (Fig. 1(a)), with an ultrathin thickness of 180 μm (Fig. S1 in the Electronic Supplementary Material (ESM)), high deformation adaptation (Fig. 1(b)) and stretchability (Fig. 1(c)), as well as high transparency (transmittance of $\geq$ 76.5% in wavelengths from 450 to 850 nm) (Fig. 1(d)). The stretchable electrode (thickness: 15 μm, Fig. S1 in the ESM) was designed through an electrode engineering strategy, which was achieved via layer-by-layer spin-coating of Ag NWs/$T_3C_2T_x$ MXene/Ag NWs on a pre-stretched plasma-etched PDMS layer and then releasing the strain to create a wrinkled surface with cracks (thickness of the AMA conductive layer: ~ 75 nm; wrinkle height: ~ 450 nm) (Fig. 1(e) and Fig. S2 in the ESM). The AMA conductive layer preserves the crystal structures of the $T_3C_2T_x$ MXene and Ag NWs (Fig. S3 in the ESM), indicating that it has the properties of both nanomaterials. The plasma etching of the polydimethylsiloxane (PDMS) surface improved the hydrophilicity and roughness (Fig. S4 in the ESM), which are conducive to the adhesion of the conductive layer. The surface roughness of the designed PDMS-AMA electrode is largely enhanced (increased by ~ 178 times) compared with the pristine PDMS layer (Fig. S4 in the ESM).

The PAT ionogel electrolyte was synthesized through photopolymerization with a one-pot multistep process, which possesses an amorphous structure (Fig. S5 in the ESM), high transparency (transmittance of $\geq$ 92.5% in wavelengths from 450 to 850 nm) (Fig. 1(d)), along with excellent stretchability (elongation at break: 1124.3%), high mechanical strength (maximum tensile stress: 0.478 MPa), toughness (2243.6 kJ·m^{-3}), and tear resistance (fracture energy: 1456.3 kJ·m^{-2}) (Fig. S6 and Note S1 in the ESM). The PAT ionogel electrolyte endows the ionic temperature sensor with enhanced stretchability compared with the PDMS-AMA electrode (elongation at break: 180.3% vs. 137.8%) (Fig. S7 in the ESM). Additionally, the PAT ionogel possesses abundant polar groups (e.g., amide groups) (Fig. S8 and Note S1 in the ESM) that are in favor of the adhesion to the electrode (Fig. S9(c) in the ESM). Note that more detailed information for the fabrication of the AMA electrode, PAT ionogel, and AMA-PAT ionic temperature sensor can be seen in Methods.

It is found that the PDMS-AMA electrode has an adhesion strength to the PAT ionogel electrolyte that is ~ 3.7 and ~ 6.9 times stronger than the PDMS-AA electrode (spin-coating Ag NWs for two times without inserting the MXene layer) and pristine PDMS layer, respectively (Fig. 1(f) and Fig. S9(b) in the ESM). Given that the surface roughness of the PDMS-AMA and PDMS-AA electrodes is very close (76.1 and 79.2 nm, respectively) (Fig. S4 in the ESM), the increased adhesion strength to the PAT ionogel of the PDMS-AMA electrode can be mainly because the introduced MXene has surface terminal groups (–O, OH, and –F) (Fig. 1(g)) that can form hydrogen bonds with the PAT ionogel (Figs. S8 and S9(c) in the ESM). Note that the full X-ray photoelectron spectroscopy (XPS) spectrum of MXene can be found in Fig. S10 in the ESM, and a more detailed explanation for the superior adhesion of the PDMS-AMA electrode to the PAT ionogel can be found in Note S2 in the ESM. The excellent adhesion between the PDMS-AMA electrode and PAT ionogel electrolyte allows the formation of a reliable and stable electrode/electrolyte interface that can help maintain a stable electric double-layer structure under deformation, ensuring the reliability of the sensing performance of the AMA-PAT ionic temperature sensor. Moreover, the AMA-PAT ionic temperature sensor with the PDMS-AMA electrode has a conspicuously higher temperature sensitivity (~ 5.3 and ~ 7.9 times higher) than the AA-PAT and M-PAT ionic temperature sensors with the PDMS-AA electrode and PDMS-M electrode (only spin-coating a MXene layer on the PDMS), respectively (Fig. 1(h)). The AMA-PAT ionic temperature sensor also possesses a strain-insensitive property that can maintain its sensing performance under strain, which enables it to accurately monitor temperature on deformable surfaces, demonstrating great potential for health monitoring on deforming surfaces (Fig. 1(i)). More details for the

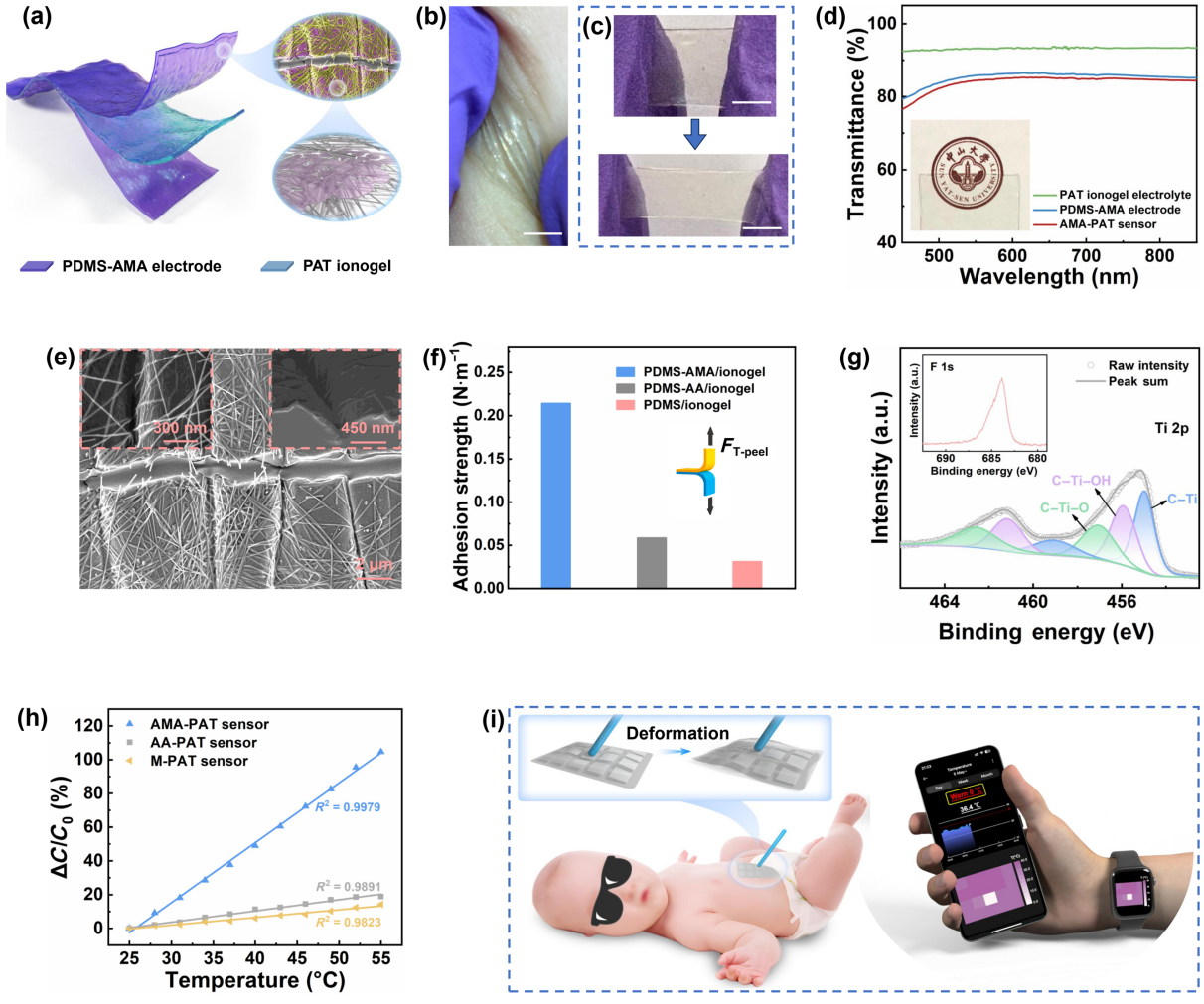

Figure 1 Design and basic characteristics of the AMA-PAT ionic temperature sensor. (a) Schematic diagram of the AMA-PAT flexible temperature sensor. (b) and (c) A typical AMA-PAT sensor is mounted on the skin under twisting and stretching. Scale bar, 0.5 cm. (d) Transmittance of the PAT ionogel, PDMS-AMA electrode, and AMA-PAT sensor. Inset: photograph of the sensor over a university logo. (e) SEM images of the PDMS-AMA electrode. (f) Adhesion strength of the PDMS-AMA electrode, PDMS-AA electrode, and pure PDMS to the PAT ionogel. (g) High-resolution Ti 2p and F 1s XPS spectra of $Ti_3C_2T_x$ MXene. (h) Relationships between the relative capacitance changes and temperature of the AMA-PAT, AA-PAT, and M-PAT ionic temperature sensors. (i) Schematic illustration showing the AMA-PAT ionic temperature sensor array monitoring the skin temperature and temperature of an external touch for the deforming belly during respiration.

enhanced sensing performance through the electrode engineering strategy via the insertion of a MXene layer between two Ag NWs layers and the strain-insensitive sensing performance of the AMA-PAT ionic temperature sensor will be presented in the following paragraphs.

2.2 MXene enhanced temperature sensing performance

The electrode engineering strategy of the introduction of MXene between two layers of Ag NWs enhances the sensing performance of the ionic temperature sensor, with the maximum sensitivity (3.55 %·℃$^{-1}$) appearing at Ag NWs:MXene = 1:1/2 (ratio of mass concentration) (Figs. 2(a) and 2(b)). This enhanced performance could be mainly because of two reasons. First, the addition of MXene into the PDMS-AA electrode lowers the surface potential and suppresses the adsorption of ions on the electrode surface (Figs. 2(c)–2(e) and Fig. S11 in the ESM), correspondingly reducing the original capacitance (C_0) of the ionic temperature sensor (at room temperature (RT) of 25 ℃ (Fig. 2(c)). Note that as the amount of MXene goes up, the electrode's surface potential and the C_0 experience slight increases (when Ag NWs:MXene = 1:1) during the declining trend, which could result from the nonuniform distribution caused by the aggregation of MXene sheets (Fig. S11(d) in the ESM). The surface potential of the electrode with Ag NWs:MXene = 0:1 (i.e., the PDMS-M electrode) is too small to be detected by the test instrument. Second, MXene constrains neutral ion pairs of [EMIM]TFSI through hydrogen bonding on the electrode surface, whose dissociation is enhanced with the increasing temperatures [31, 32], leading to an increase in free charged ions adsorbing on the electrode surface. As shown in the FTIR spectra in Fig. 2(f), the characteristic peaks associated with the imidazole ring of the ionic liquid modified MXene exhibit noticeable blue shifts compared with the pristine ionic liquid: The peaks of the C–N (CH_3(N)) stretching show conspicuous blue shifts (from 611 to 614 and 1170 to 1182 cm^{-1}), and the peaks of C=N and C–H stretchings also show blue shifts (from 1573 to 1574 and from 3157 to 3160 cm^{-1}, respectively). The Raman spectra show that the peak assigned to Ti–O vibration, indicating the attachment of –O and –OH undergoes a clear red shift from 200 to 196 cm^{-1} (Fig. 2(g)). The FTIR and Raman results prove that the MXene forms strong interactions with the ionic liquid, which can be the

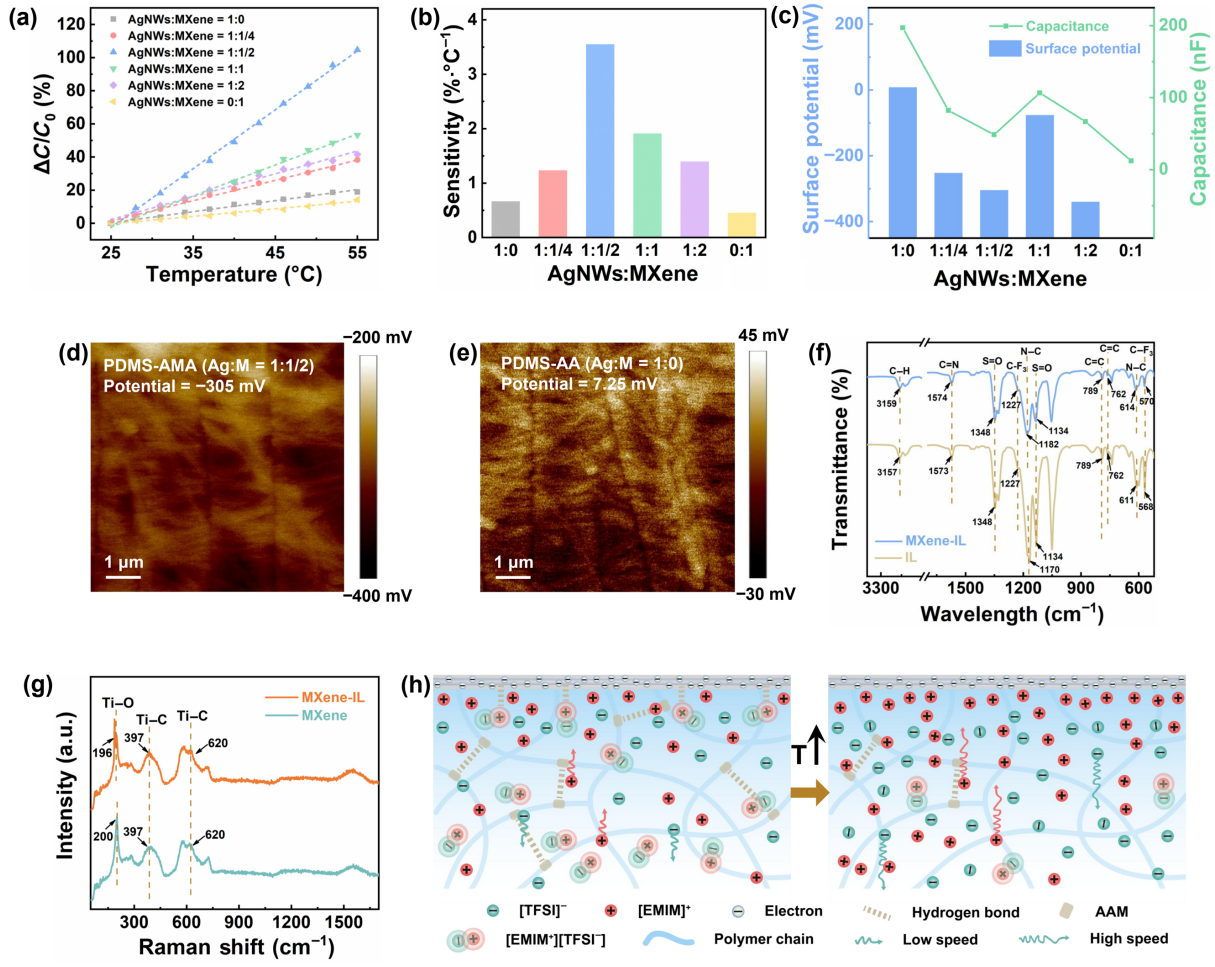

Figure 2 MXene enhanced temperature sensing performance. (a) and (b) Relationships between the relative capacitance changes and temperature of the ionic temperature sensors with the electrodes having different amounts of MXene inserted between two Ag NWs layers. (c) Surface potentials of the electrodes having different amounts of MXene inserted between two Ag NWs layers and the original capacitances of the corresponding ionic temperature sensors. (d) and (e) AFM images showing the surface potentials of the PDMS-AMA and PDMS-AA electrodes. (f) and (g) FTIR and Raman spectra of the pure ionic liquid (IL) and IL-modified MXene. (h) Schematic illustration showing the temperature-sensing mechanism of the AMA-PAT ionic temperature sensor. Three main factors: weakened constraint of polymer chains, accelerated ion transportation, and increased free charged ions. Specifically, the introduction of MXene suppresses ion adsorption while binding neutral ion pairs, which release more free charged ions as the temperature rises.

hydrogen bonding between the –OH of MXene and –N of ionic liquid [33–37].

To investigate whether this electrode engineering strategy can be applied to temperature sensors with other kinds of gel electrolytes, the temperature sensors with thermoplastic polyurethane (TPU)/[EMIM]TFSI ionogel, PAAm hydrogel, and PAAm/NaCl ionic hydrogel as electrolytes have been fabricated and examined. It is found that the electrode engineering strategy of MXene insertion can also enhance the sensing performance of the temperature sensor with the TPU ionogel as the electrolyte (Fig. S12(a) in the ESM); however, it has little effect on the sensing performance of the temperature sensors with the PAAm hydrogel and PAAm/NaCl ionic hydrogel as electrolytes (Figs. S12(b) and S12(c) in the ESM), which could be because the PAAm hydrogel has hardly any free ions, and NaCl undergoes complete ionization in the PAAm/NaCl ionic hydrogel during the whole sensing temperature range, respectively. This result further proves the mechanism for the enhanced sensitivity by the insertion of MXene in the AMA-PAT ionic temperature sensor, and suggests that it is applicable to ionic temperature sensors whose neutral electrolyte ion pairs can bond with MXene and have enhanced ion dissociation with increasing temperatures. Note that the M-PAT ionic temperature sensor has a smaller sensitivity than the AA-PAT ionic temperature sensor, which can be mainly because the resistance of the PDMS-M electrode is too large (over hundreds of MΩ), failing to sufficiently adsorb the augmented free ions at the rising temperature. The capacitances of the ionic temperature sensors in this work were measured at a frequency of 100 Hz, where the capacitances mainly originate from the electric double-layer charge storage mechanism (Fig. S13 and Note S3 in the ESM).

Combining the above results and discussions, the temperature sensing mechanism for the AMA-PAT ionic temperature sensor can be mainly attributed to the following three factors (Fig. 2(h)). First, the constraint of polymer chains weakens with increasing temperatures. The storage modulus and loss modulus of the PAT ionogel decrease from 19,270 and 8388 to 12,830 and 3538 Pa as the temperature rises from 25 to 55 °C, respectively (Fig. S14 in the ESM), demonstrating that the strengths of the connection among polymer chains as well as interactions between polymer chains and ions decline, delivering more free space for ion migration. Second,

the charge transfer resistance reduces and ion mobility enhances with the increasing temperatures (Fig. S15 in the ESM), bringing about accelerated ion transportation at higher temperatures. Third, the dissociation of ion pairs augments with increasing temperatures, resulting in increased free charged ions. Particularly, the introduction of MXene suppresses the ion adsorption but meanwhile traps neutral ion pairs, which release more free charged ions on the electrode surface as the temperature rises. The ion conductivity of the PAT ionogel increases with the elevating temperature (from 2.48 to 5.06 mS·cm^{-1} as the temperature elevates from 25 to 55 °C) (Fig. S16 in the ESM), which corresponds to the faster ion migration and larger ion concentration. Note that the resistances of the PDMS-AMA and PDMS-AA electrodes have little change during the temperature sensing range (Fig. S17 in the ESM).

2.3 Characterization of the performance of the AMA-PAT ionic temperature sensor

Besides the high sensitivity with excellent linearity (R^2 = 0.9981) (Figs. 1(h) and 2(a)), the transparent stretchable AMA-PAT ionic temperature sensor possesses high resolution, reproducibility, stability, and reliability. As shown in Fig. 3(a), the AMA-PAT ionic temperature sensor can accurately detect the tiny step-wise temperature change of 0.1 °C with excellent linearity (R^2 = 0.9995), demonstrating a high resolution of at least 0.1 °C. The output capacitance responding to a given temperature during the reciprocating heating/cooling process and cyclic sensing test is almost the same (Figs. 3(b) and 3(c)), proving high reproducibility. The response time and recovery time are approximately 36 and 40 s, respectively (Fig. 3(d)). Note that the response/recovery time is mainly impacted by the ion transport process and heat diffusion. Accelerating the ion movement through methods such as the optimization of the ionogel's polymer network and facilitating the heat diffusion through methods such as the creation of porous structures could help achieve faster response/recovery time. The sensor exhibits highly repeatable and reliable response to temperature changes, with the sensing performance nearly unchanged for 45 cycles of temperature variation (Fig. 3(e)). Moreover, the sensing performance is nearly unchanged under various humidity conditions for 8 h or when soaked in sweat for 8 h (Fig. 3(f) and 3(g)). The AMA-PAT ionic temperature sensor also maintains its sensing performance under pressure of < 0.5 kPa (Fig. 3(h)). Note that the corresponding output capacitances under

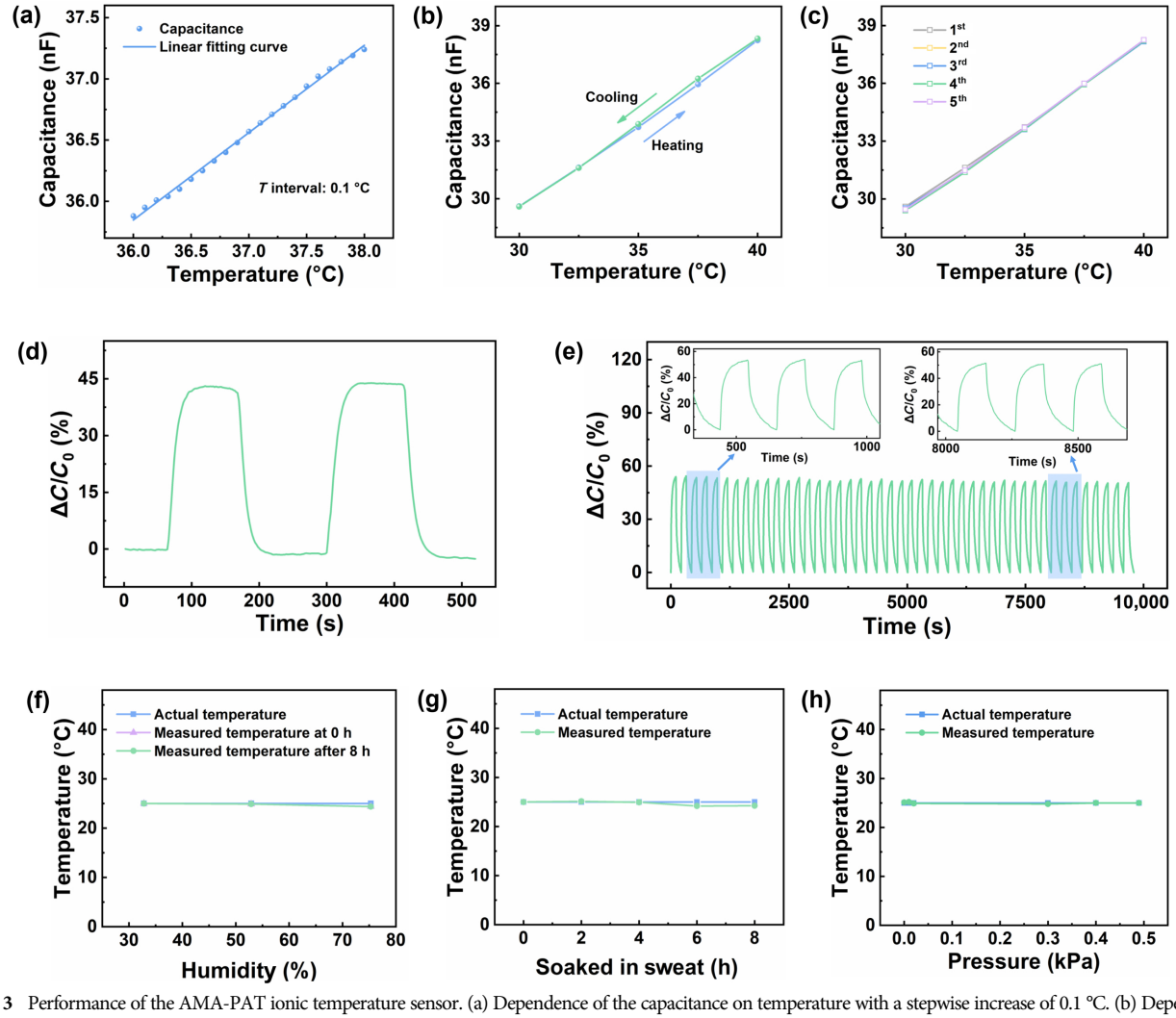

Figure 3 Performance of the AMA-PAT ionic temperature sensor. (a) Dependence of the capacitance on temperature with a stepwise increase of 0.1 °C. (b) Dependence of the capacitance on temperature under the reciprocating heating/cooling cycle. (c) Repeatable temperature sensing under cyclic heating. (d) Typical time-response curve to temperature. (e) Cyclic time-response curve to temperature. (f)–(h) Stable temperature sensing performance under different humidity (for 8 h), sweat immersion (for 8 h), and various pressures (0–0.5 kPa).

the influence of humidity, sweat, and pressure can be found in Figs. S18 and S19 in the ESM. In addition, the AMA-PAT ionic temperature sensor presents antifreeze property and high thermal stability, with a wide working temperature range from −35 to 70 °C (Fig. S20 in the ESM). These environmental tests demonstrate the high reliability of the AMA-PAT ionic temperature sensor for practical applications. Note that the sensing range primarily tested in this work is 25–55 °C, which is sufficient for wearable applications such as on-skin epidermal electronics.

2.4 Strain-insensitive sensing performance of the AMA-PAT ionic temperature sensor

The transparent stretchable AMA-PAT ionic temperature sensor possesses strain-insensitive sensing performance, with its sensitivity nearly unchanged under strain from 0 to 50% (Fig. 4(a)). To demonstrate this strain-insensitive sensing property, an AMA-PAT ionic temperature sensor was worn on the finger joint of a person, and it shows that the temperature sensing performance remains stable under various finger motions (Fig. 4(b)). Note that the corresponding output relative capacitance change ($\Delta C/C_0$) can be found in Fig. S21 in the ESM. As mentioned above, the AMA-PAT ionic temperature sensor operates as an electric double-layer capacitor, whose capacitance can be given as [38]

$$C_{\text{total}} = \frac{C_{\text{EDL}}}{2} = \frac{1}{2}\frac{C_{\text{HS}}C_{\text{D}}}{C_{\text{HS}}+C_{\text{D}}} = \frac{1}{2}\frac{\varepsilon_0\varepsilon_{\text{r}}}{x_{\text{HS}}+x_{\text{D}}}S_{\text{eff}} = \frac{1}{2}\frac{\varepsilon_0\varepsilon_{\text{r}}}{x_{\text{HS}}+\sqrt{\dfrac{\varepsilon_0\varepsilon_{\text{r}}RT}{2F^2c_{\text{i}}}}}S_{\text{eff}} = \frac{1}{2}C_{\text{u}}S_{\text{eff}} \quad (1)$$

where C_{total}, ε_0, and ε_r are the total capacitance of the device, vacuum permittivity, and permittivity of the PAT gel, respectively. C_{EDL}, C_{HS}, C_{D}, x_{HS}, and x_{D} are each electrode's electric double-layer capacitance, capacitance of the Helmholtz or Stern layer, capacitance of the diffuse layer, thickness of the Helmholtz or Stern layer, thickness of the diffuse layer, respectively. R, F, c_{i}, and T are the universal gas constant, Faraday constant, ion concentration in the bulk electrolyte, and temperature, respectively. S_{eff} is the effective overlap surface area of the electrode, and C_{u} is the capacitance per unit effective overlap surface area of the electrode.

When the device structure, electrode and electrolyte materials are determined, C_{u} is only related to T, and C_{total} is only related to T and S_{eff}. When the device is stretched, owing to the Poisson effect, the thickness of the device shrinks, and the total surface area expands. The reduction in the thickness of the device does not affect the C_u because the thickness of the electric double layer near the electrode surface is far thinner than the device thickness. The

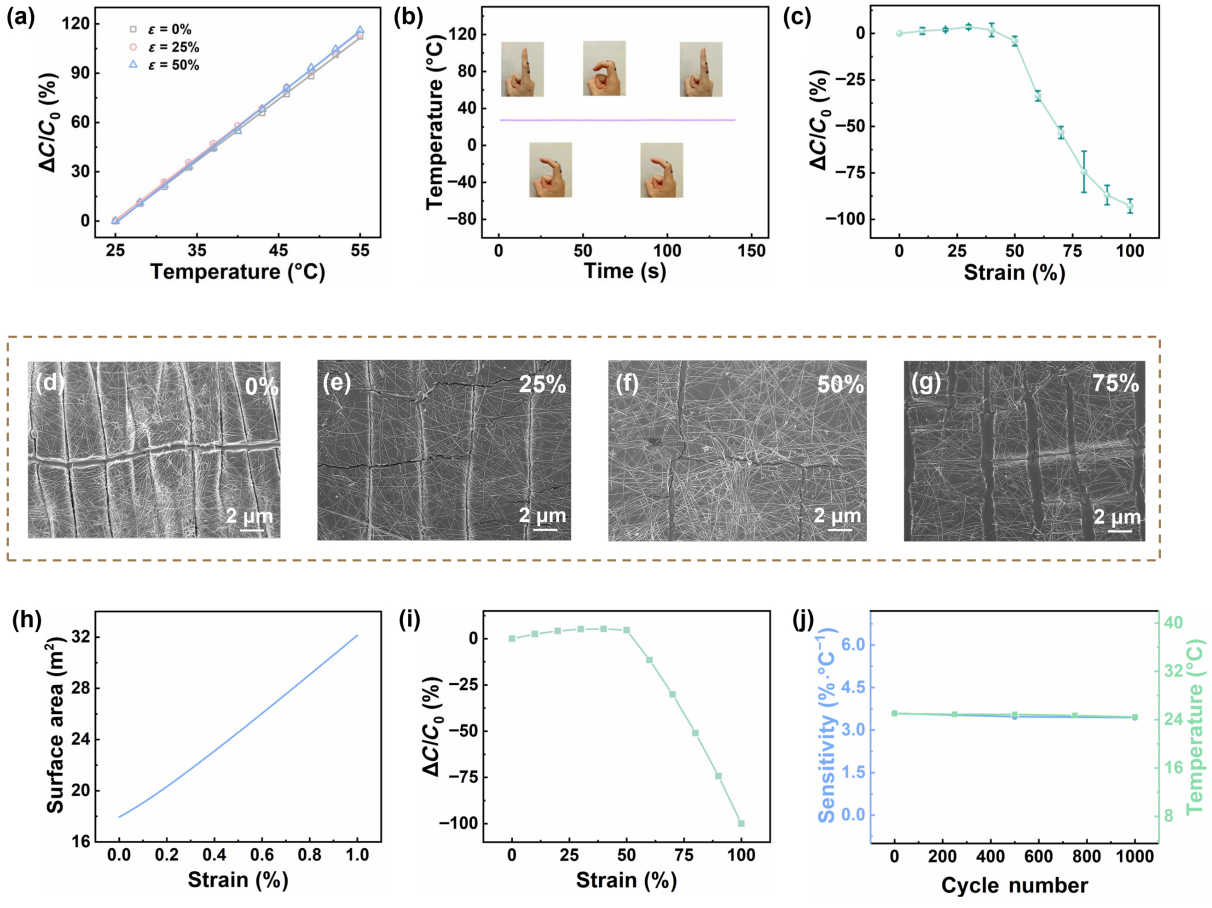

Figure 4 Strain-insensitive sensing performance of the AMA-PAT ionic temperature sensor. (a) Relationships between the relative capacitance change and temperature under different strains. (b) Stable temperature sensing of the sensor mounted on a finger joint under various finger motions. (c) Relative capacitance change under strain of 0–100%. (d)–(g) SEM images showing the morphologies of the PDMS-AMA electrode under strain of 0, 25%, 50%, and 100%. (h) Relationship between the total surface area and strain acquired from the theoretical simulation. (i) Relative capacitance change under strain of 0–100% obtained from theoretical simulation. (j) Sensitivities of, and measured temperatures of the testing compartment by the AMA-PAT ionic temperature sensor under cyclic tensile strain of 50% during 1000 cycles. Note: The temperature of the testing compartment was maintained at 25 °C.

expansion of the electrode area is expected to increase C_{total}. But the actual values of C_{total} are nearly unchanged under various strain ($\leq$ 50%) at the same temperature (Fig. 4(c)), which can be attributed to the fact that the enlarging strain widens the cracks on the electrode surface and increasingly cuts off the conductive paths for electrons of the electrode (Figs. 4(d)–4(g)), counteracting the expanding surface area by the strain. As a result, the effective overlap surface area of the electrode is nearly unchanged during the stretching, and the capacitances under various strains remain nearly unchanged at the same temperature, leading to the strain-insensitive sensing performance. Note that the electrode resistance of the AMA-PAT sensor increases from about 120 to 1300 Ω as the strain increases from 0 to 50% (Fig. S22 in the ESM). Since the electrode resistance changes little with temperature variation (Fig. S17 in the ESM) and the equivalent series resistance was over 3124 Ω during the sensing range (Fig. S15 in the ESM), much larger than the electrode resistance, the effect of the electrode resistance on the capacitance of the AMA-PAT sensor within 50% strain could be neglected. As the strain further increases over 50%, the electrode resistance undergoes an abrupt increase, leading to sharply reduced C_0 (Fig. 4(c)) and loss of the strain-insensitive property (Fig. S23 in the ESM). Strategies such as optimizing the conductive network by employing locally bundled dual ligands modified Ag NWs to extend the resistance breakpoint under strain may help further widen the strain-insensitive range of the sensor. The degree of the prestrain of the electrode impacts the C_0 and the sensitivity of the sensor. As the prestrain increases from 0 to 100%, the sensitivity gradually decreases while the C_0 first increases and then decreases, with the maximum value achieved when the prestrain is 50% (Fig. S24 in the ESM). Considering the sensitivity, stretchability, and application scenarios, a prestrain of 50% was employed in this work, which is sufficient for wearable applications with moderate stretchability requirements [39, 40].

To quantitatively describe the crack counteraction-enabled strain-insensitive property, numerical simulations were implemented in COMSOL multiphysics using the finite element method. The total surface area S of the electrode expands with the increasing strain as follows (Fig. 4(h) and Fig. S25 in the ESM)

$$S = S_0 + A\varepsilon \tag{2}$$

where S_0 is the total surface area without strain, ε is the applied strain, and A is a constant representing the stretching coefficient. Considering the influence function $K(\varepsilon)$ of the electrode cracks, the effective overlap surface area of the electrode can be given as

$$S_{eff} = (S_0 + A\varepsilon)\,K(\varepsilon) \tag{3}$$

To quantitatively explain the influence of the electrode cracks on the effective overlap surface area S_{eff} and C_{total}, the influence function $K(\varepsilon)$ can be given as

$$K(\varepsilon) = \begin{cases} 1 - r_1\varepsilon, & 0 \leq \varepsilon < 0.5 \\ 1 - 0.5r_1 - r_2(\varepsilon - 0.5), & 0.5 \leq \varepsilon \leq 1 \end{cases} \tag{4}$$

where r_1 and r_2 are the fracture coefficients under unit strain for the two stages. Then, a model of the electric double-layer capacitor corresponding to the ionic temperature sensor was established (Fig. S26 in the ESM), where an applied voltage between the two electrodes leads to a potential drop in the ionogel (Fig. S27(a) in teh ESM), the equivalent surface charge density of the electric double-layer capacitor increases with the applied voltage (Fig. S27(b) in teh ESM), and ion concentrations decrease with the increasing distance from the electrode surface at various applied voltages (Fig. S28 in the ESM). Consequently, the C_{total} of the device can be calculated as

$$C_{total} = \frac{1}{2}\frac{\varepsilon_0\varepsilon_r S_{eff}}{x_{HS} + x_D} = \frac{1}{2}\frac{\varepsilon_0\varepsilon_r(S_0 + A\varepsilon)K(\varepsilon)}{x_{HS} + x_D} = \frac{1}{2}\frac{\varepsilon_0\varepsilon_r(S_0 + A\varepsilon)K(\varepsilon)}{x_{HS} + \sqrt{\frac{\varepsilon_0\varepsilon_r RT}{2F^2 c_i}}} \tag{5}$$

The calculated capacitances of the AMA-PAT ionic temperature sensor from the theoretical simulation have the same changing trend as the experimental results with the enlarging applied strain (Fig. 4(i)), quantitatively verifying the crack counteraction mechanism for the strain-insensitive sensing performance. Note that more detailed information for the theoretical simulation can be found in Note S4 in the ESM.

The strain-insensitive property of the AMA-PAT ionic temperature presents high cyclic stability, with the temperature sensitivity of the sensor, the measured temperature of the testing compartment by the sensor, and the corresponding capacitance of the sensor all nearly unchanged during 1000 cycles of tensile strain at 50% (Fig. 4(j) and Fig. S29 in the ESM). Note that the temperature of the testing compartment was maintained at 25 °C. The high stability of the sensor under cyclic strain can be mainly because the excellent elasticity of the PDMS, along with the high adhesion strength of the PDMS-AMA electrode to the PAT ionogel (Fig. 1(f) and Fig. S9 in the ESM), ensures that the AMA-PAT ionic temperature sensor can return to its original state after stretching.

2.5 Applications of the AMA-PAT ionic temperature sensor

The AMA-PAT ionic temperature sensor shows great potential for applications in various areas such as healthcare, prosthetics, sports, and robotics. Besides the application of monitoring body temperature exhibited in Fig. 4(b), which presents stable sensing performance under deformation from finger motion, applications of the smart prosthetic hand (temperature warning and human-prosthetic interaction), motion tracking, and temperature monitoring of deforming surface were also demonstrated. As shown in Fig. 5(a) and Movies S1–S3 in the ESM, a temperature alarm system based on the AMA-PAT ionic temperature sensor was constructed with the sensor worn on a prosthetic hand, which can protect the prosthetic hand from extreme temperatures that hurt the human body/skin. Benefitting from the fact that the capacitance of the AMA-PAT sensor monotonically increases with the increasing temperature from −35 to 70 °C (Fig. S20(a) in the ESM), the lower and upper temperature limits of 5 and 50 °C (corresponding capacitances of the amounted device were 7 and 24 nF), respectively, were set to a circuit board controlled by a capacitive switch. Note that the lower and upper temperature limits were set to protect the person wearing the prosthetic hand from potential harm posed by cold and hot touches. Studies have found that the threshold temperature for pricking pain in human skin is 43.9 ± 0.7 °C [41], and prolonged exposure to temperatures below 0 °C will result in frostbite injury [42]. Considering the heat diffusion distance from the prosthetic hand to the wearer's body/skin and a normal living environment of human beings, 5 and 50 °C were set as the lower and upper temperature limits, respectively, and touching temperatures on the prosthetic hand

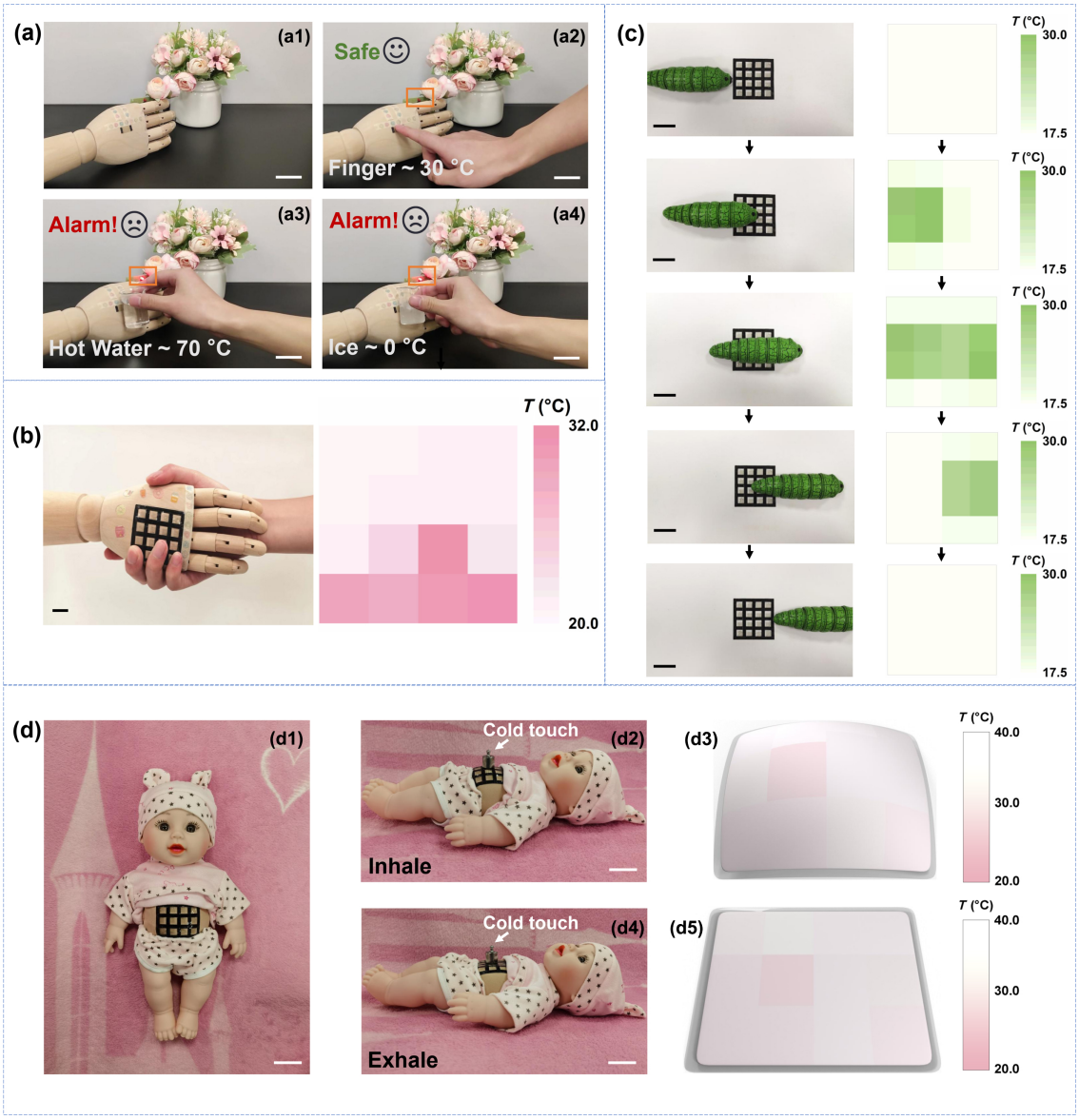

Figure 5 Applications of the AMA-PAT ionic temperature sensor. (a) A temperature alarm system based on a sensor detecting the temperature of finger touch and delivering warnings of hot/cold temperatures: (a1) without touch, (a2) safe touch from a human finger, ((a3) and (a4)) alarm touches from hot water and crushed ice. Scale bar, 5 cm. (b) A prosthetic hand with a temperature sensor array detecting the temperature distribution from handshaking with a person. Scale bar, 2 cm. (c) A temperature sensor array monitoring the motion path of a warm electric worm. Scale bar, 3 cm. (d) A temperature sensor array worn on a doll's belly monitoring the temperature during breathing with the belly shrinking and expanding: (d1) front view, (d2) inhale, (d3) temperature map during inhale, (d4) exhale, and (d5) temperature map during exhale. Scale bar, 5 cm.

within these two temperature limits were defined as safe. More details for the circuit board can be found in Fig. S30 in the ESM. When a human finger touched the sensor, it detected the finger's temperature of 30 °C, recognizing as "Safe". When a beaker containing hot water of ~ 70 °C or crushed ice of ~ 0 °C touched the sensor, warnings were activated with the buzzer ringing and light-emitting diode (LED) illuminating, recognizing as "Alarm".

Then, an AMA-PAT sensor array with 4 × 4 pixel devices was fabricated and worn on a prosthetic hand, which can accurately detect the temperature information in contact from handshaking with a person (Fig. 5(b)). This sensor array was then applied for motion tracking. As shown in Fig. 5(c), when a warm electric worm (a piece of heating pad was attached to its bottom surface) crawled through the sensor array, its moving path can be accurately detected. Furthermore, owing to the strain-insensitive sensing property, the AMA-PAT sensor can accurately monitor the temperature of the deforming surface. As shown in Fig. 5(d), a 4 × 3 AMA-PAT sensor array was worn on the belly of a doll to monitor its body temperature and external touch during breathing. The doll's belly with the attached sensor array bulged on inhalation and sucked in on exhalation (Figs. 5(d2) and 5(d4)). Despite such deformation during breathing, the sensor array mounted on the doll's belly maintained its accurate detection of the temperature distribution of the doll's belly touched by a cold block during breathing, with the belly expanding and shrinking (Figs. 5(d3) and 5(d5)). Note that the corresponding $\Delta C/C_0$ distributions for the sensor array in these applications can be found in Fig. S31 in the ESM.

3 Conclusions

In summary, an ionic temperature sensor is developed with high transparency (transmittance ≥ 76.5%) and stable sensing performance under strain of ≤ 50%. An electrode engineering strategy of inserting MXene into two Ag NWs layers was discovered to be capable of enhancing the sensing performance, with a sensitivity reaching ~ 5.3 times higher than the sensor without inserting MXene in the electrode. This is mainly because the insertion of MXene lowers the surface potential and suppresses the adsorption of ions on the electrode surface, but meanwhile, MXene bonds with neutral ion pairs whose dissociation enhances with temperature, releasing more free ions on the electrode surface as the temperature rises. This MXene-enhanced performance is applicable to ionic temperature sensors having neutral electrolyte ion pairs that can bond with MXene and have augmented ion dissociation as the temperature elevates. The strain-insensitive sensing property is mainly owing to a crack counteraction mechanism, where the promoting effect of the expanding electrode surface area with the extending strain on the capacitance is counteracted by the decreased conductive paths due to the widening cracks. This crack counteraction mechanism was quantitatively verified through systematic theoretical simulations. The transparent strain-insensitive stretchable ionic temperature sensor was demonstrated for applications of body temperature monitoring, smart prosthetic hand, motion tracking and temperature monitoring of deforming surface, which can accurately detect skin temperature despite body motion, warn the touch of hot/cold temperatures through constructing an alarm system, record the touch information from handshaking, track the motion path of a warm electronic worm and monitor the temperature of a deformable belly during breathing. The ionic temperature sensor exhibits high environmental reliability with maintained sensitivity under sweat, various humidity conditions and pressures. The strain-insensitive sensing performance also presents high cyclic stability with the sensitivity nearly unchanged over 1000 cycles of 50% strain. For future research, the sensitivity of the ionic temperature sensor can be further enhanced through routes such as exploiting an ionogel with a bigger change in the dielectric constant per unit temperature; the response/recovery time can be further shortened through strategies such as optimizing the ionogel's polymer network to accelerate the ion movement and creating porous structures to facilitate the heat diffusion; and the adhesion of the sensor to the body or other electronic components can be improved through methods such as surface modification of the PDMS outer layer by plasma and the mixture of adhesive additives into PDMS. This work provides new insights for the development of novel stretchable sensors and offers fundamental guidance for the strain-insensitive property of stretchable electronics.

4 Methods

4.1 Materials

All chemicals were of analytical grade and were utilized as received without further purification. Acrylamide (AAm, ≥ 99%) and 2-hydroxy-4'-(2-hydroxyethoxy)-2-methylpropiophenone (I_{2959}, 98%) were purchased from Shanghai Titan Scientific Co., Ltd. 2,2,2-Trifluoroethyl acrylate (TFEA, 98%) was purchased from Shang Fluoro. [EMIM][TFSI] (98%) was purchased from Monils Chemical (Shanghai) Co., Ltd. Silver nanowires (1 wt.% IPA, D = 30 nm·L^{-1} = 30 μm) was purchased from Zhongke Leiming (Beijing) Technology Co., Ltd. Titanium aluminum carbide (Ti_3AlC_2, ≥ 99%) was purchased from Laizhou Kai Kai Ceramic Materials Co., Ltd. Lithium fluoride (LiF, 99%), polyvinyl alcohol (PVA, 1788), ammonium persulphate (APS, ≥ 99.99%), and N,N'-methylenebisacrylamide (MBAA, ≥ 97%) were purchased from Shanghai Aladdin Biochemical Technology Co., Ltd. Hydrochloric acid (HCl, 36-38%) was purchased from Guangzhou Chemical Reagent Factory. N,N,N',N'-Tetramethylethylenediamine (TEMED, ≥ 99%) was purchased from Thermo Fisher Scientific, Inc. PDMS (Sylgard 184) was purchased from Dow Chemical (China) Co., Ltd. TPU (EG-85A-B20) was purchased from Lubrizol Special Chemical (Shanghai) Co., Ltd.

4.2 Fabrication of the ionic temperature sensors

4.2.1 *Synthesis of $Ti_3C_2T_x$ MXene*

The $Ti_3C_2T_x$ MXene (hereinafter referred to as MXene) was synthesized by stripping the MAX phase (Ti_3AlC_2) through a mild LiF/HCl etching method. First, 1.98 g of LiF powder was poured into 30 mL of 9 M HCl solution and dissolved for 5 min, followed by slowly adding 1 g of Ti_3AlC_2 powder. After stirring for 30 min, the mixed solution was reacted at 40 °C for 45 h. Subsequently, the supernatant was removed by decantation, and the sediment was washed several times with deionized water by centrifugation until the pH > 4. The multilayer MXene sediment was then dispersed in 150 mL of deionized water, and the solution was sonicated for 1 h in an ice bath protected by an Ar flow to obtain MXene with monolayer or few layers. Finally, after centrifuging at 3500 rpm for 1 h, the MXene suspension for spin coating was obtained.

4.2.2 *Preparation of the stretchable electrodes*

A PVA sacrificial layer was first prepared on a clean glass substrate, followed by spin-coating the PDMS fluid on the PVA layer. After the PDMS was cured, the PVA layer was dissolved and removed by deionized water to obtain the PDMS layer. The PDMS layer was then stretched to a strain of 50%, and the surface of the stretched PDMS layer was etched via plasma treatment. Next, a conductive film was formed on the pre-stretched PDMS via spin coating of Ag NWs, MXene, and Ag NWs (AMA) in turn at 1000 rpm for 60 s each time, followed by slowly releasing the prestrain of the PDMS layer. Then, the obtained PDMS-AMA layer was placed in a vacuum oven overnight to remove the residual solvent. Finally, the stretchable PDMS-AMA electrode was acquired. Note that the mass concentration of the Ag NWs suspension for spin coating was 2 mg·mL^{-1}. The amount of MXene added between the two Ag NWs layers was regulated by adjusting the mass concentration of the MXene suspension for spin coating. The PDMS-AA stretchable electrode was fabricated by spin coating Ag NWs for two times without the addition of MXene, and the PDMS-M stretchable electrode was fabricated by only spin coating MXene (1 mg·mL^{-1}) for one time.

4.2.3 *Preparation of the ionogel electrolytes*

Preparation of the PAT ionogel: 0.2843 g of AAm, 1.2327 g of TFEA (as two monomers), and 7.6 mg of I_{2959} (as the initiator, 0.5 wt.% with respect to monomers) were first dissolved in 2.2755 g of ionic liquid [EMIM]TFSI under magnetic stirring to obtain a homogenous solution. Then, after bubbling with Ar for 10 min to remove oxygen, the solution was poured into a homemade rectangular module with a silicone-rubber frame (height: 150 μm)

between a glass plate and a PET plate, followed by photoinitiated polymerization under ultraviolet (UV) light (2 mW·cm^{-2}, 365 nm) for 2 h in an inert-atmosphere glove box that maintained low oxygen and humidity levels. Finally, the PAT ionogel with a thickness of 150 μm was obtained. Note that the reaction formula of the PAT ionogel can be found in Fig. S8(c) in the ESM.

Preparation of the TPU ionogel gel: Initially, 1.5 g of TPU particles was dissolved in THF with a mass ratio of 1:5 at 60 °C for 1 h, and 2.2755 g [EMIM][TFSI] was added to form a homogeneous viscous solution. Next, 3 mL of the acquired solution was transferred to a beaker; then, it was first placed in a fume cupboard overnight to evaporate most of the THF solvent, and subsequently put into a vacuum oven to thoroughly remove the solvent. Finally, the TPU ionogel was obtained. The obtained TPU ionogel had the same mass concentration as the PAT ionogel.

Preparation of the PAAm hydrogel: 1.4 g of AAm (as a monomer), 7 mg of APS (as the initiator, 0.5 wt.% with respect to the monomer), and 1.4 mg MBAA (as the cross-linking agent, 0.5 wt.% with respect to the monomer) were dissolved in 5 mL of deionized water. Then, the acquired solution was transferred to an ice bath and stirred for 10 min. Next, 5 μL of TEMED was continuously added, accompanied by quick stirring. The resulting solution was then poured into a polytetrafluoroethylene (PTFE) mold. After 1 h of reaction at room temperature, the PAAm hydrogel was obtained.

Preparation of the PAAm/NaCl ionic hydrogel: The PAAm/NaCl ionic hydrogel was prepared through the same processes as the PAAm hydrogel, except that 0.672 g of NaCl was additionally added during the mixing process. The obtained PAAm/NaCl ionic hydrogel had the same ionic concentration as the PAT ionogel.

4.2.4 *Construction of the sensors*

The ionic temperature sensors were assembled by sandwiching the PAT ionogel layer between two stretchable electrodes. Two copper wires were led out from the upper and lower electrodes on both sides, respectively, for the following electrical tests, and the electrical connections were protected by encapsulating a PDMS layer.

4.3 Fabrication of the AMA-PAT ionic temperature sensor array

The stretchable PDMS-AMA electrodes were first arranged on a polyvinylidene difluoride (PVDF) substrate in a 4× 4 array as the top and bottom electrodes. Copper wires were then led in each horizontal row of the bottom electrodes, as well as in each vertical row of the top electrodes. Next, the PAT ionogel was placed at the corresponding position of the bottom electrodes, and the top electrodes were subsequently assembled in alignment. After the encapsulation by PDMS and release from the PVDF substrate, the AMA-PAT ionic temperature sensor array was obtained, and the size of each temperature sensor was about 8 mm × 8 mm.

4.4 Characterization and measurement

4.4.1 *Temperature sensing tests*

The capacitances of the temperature sensors in the electrical tests were measured by an LCR meter (Microtest 6367A) at an applied voltage of 1 V under a frequency of 100 Hz. All temperatures were controlled with a thermoelectric cooler-based water-cooled temperature control platform (TLT-AT150-150, accuracy 0.01 °C).

4.4.2 *Structural and morphological characterizations*

The morphologies of all samples were characterized by scanning electron microscopy (SEM, Gemini 500) at a voltage of 5 kV. The surface roughness was tested by atomic force microscopy (AFM, Bruker). The XPS measurement was conducted on a Thermo Fisher Nexsa. The Fourier-transform infrared spectroscopy (FTIR, Nicolet 6700 spectrometer), Raman spectroscopy (Renishaw Raman microscope, laser excitation of 532 nm) and nuclear magnetic resonance spectroscopy (NMR, Bruker) were carried out to acquire the microscopic molecular structures. Note that the samples of MXene modified by ionic liquid were prepared by impregnating the MXene with ionic liquid for 24 h.

4.4.3 *Electrical tests*

The surface potentials were measured by the Kelvin probe force microscopy of an AFM (Bruker). The electrochemical impedance spectroscopy (EIS) was performed using an electrochemical workstation (CHI760) over a frequency range of 0.1 Hz–1 MHz with an amplitude of 10 mV.

4.4.4 *Mechanical and adhesion tests*

Tensile tests were performed at a strain rate of 100 mm·min^{-1} by using an electronic universal testing machine (Sansi Taige, CMT). The adhesion tests were conducted by using a force and torque measurement equipment (Mark-10) at an applied peel-off rate of 25 mm·min^{-1}, with the force-displacement data recorded by a 25 N load cell.

4.4.5 *Other characterizations*

The transmittance of light was characterized by a UV–visible-near infrared spectrophotometer (300–1000 nm). The small-angle X-ray scattering (SAXS) spectrum was measured by an SAXS instrument (Xenocs). The dynamic rheological tests were performed using a rotational rheometer (Malvern Instruments Ltd., Kinexus pro+). The glass transition temperature (T_g) and the thermal decomposition temperature of the PAT ionogel were obtained by a differential scanning calorimeter (PerkinElmer) and a thermogravimetric analyzer (209F1 Libra R), respectively.

Electronic Supplementary Material: Supplementary material (characterization of PAT ionic gels, electrode adhesion mechanisms, sensor performance, and theoretical simulations) is available in the online version of this article at https://doi.org/10.26599/NR.2026.94908861.

Data availability

All data needed to support the conclusions in the paper are presented in the manuscript and the Electronic Supplementary Material. Additional data related to this paper may be requested from the corresponding author upon request.

Acknowledgements

This work was supported by the Guangdong Natural Science Foundation for Distinguished Young Scholars (No. 2023B1515020114), the National Natural Science Foundation of China (No. 52172170), Fundamental Research Funds for the Central Universities (No. 24lgqb003), Guangdong University Innovation and Enhancement Program (No. 2024KTSCX003),

Medicine-Engineering Convergence Seed Fund (2025) at Sun Yat-sen University, and Science and Technology Projects of Guangzhou (No. 2025A04J4230).

Declaration of competing interest

All the contributing authors report no conflict of interests in this work.

Author contribution statement

F. Y. proposed the concept. F. Y. and L. Y. C. conceived the idea. L. Y. C., Y. Z., B. C., and Z. H. C. conducted the experiments. L. Y. C., J. W., Y. Z., Z. H. C., and F. Y. graphed and analyzed the data. Z. W. Z. performed the theoretical simulations. J. G. P., J. X. C., J. F. H., X. X. M., H. L. L., and G. W. Y. helped with the experiments and analysis. F. Y. and L. Y. C. wrote the paper. All authors discussed the results and commented on the manuscript.

Use of AI statement

None.

References

[1] Dai, Y. H.; Wai, S.; Li, P. J.; Shan, N. S.; Cao, Z. Q.; Li, Y.; Wang, Y. F.; Liu, Y. D.; Liu, W.; Tang, K. et al. Soft hydrogel semiconductors with augmented biointeractive functions. *Science* **2024**, *386*, 431–439.

[2] Jiang, Y.; Ji, S. B.; Sun, J.; Huang, J. P.; Li, Y. H.; Zou, G. J.; Salim, T.; Wang, C. X.; Li, W. L.; Jin, H. R. et al. A universal interface for plug-and-play assembly of stretchable devices. *Nature* **2023**, *614*, 456–462.

[3] Jung, D.; Lim, C.; Shim, H. J.; Kim, Y.; Park, C.; Jung, J.; Han, S. I.; Sunwoo, S. H.; Cho, K. W.; Cha, G. D. et al. Highly conductive and elastic nanomembrane for skin electronics. *Science* **2021**, *373*, 1022–1026.

[4] Matsuhisa, N.; Niu, S. M.; O'Neill, S. J. K.; Kang, J.; Ochiai, Y.; Katsumata, T.; Wu, H. C.; Ashizawa, M.; Wang, G. J. N.; Zhong, D. L. et al. High-frequency and intrinsically stretchable polymer diodes. *Nature* **2021**, *600*, 246–252.

[5] Yu, X. G.; Xie, Z. Q.; Yu, Y.; Lee, J.; Vazquez-Guardado, A.; Luan, H. W.; Ruban, J.; Ning, X.; Akhtar, A.; Li, D. F. et al. Skin-integrated wireless haptic interfaces for virtual and augmented reality. *Nature* **2019**, *575*, 473–479.

[6] Cui, Y. Y.; Sun, M. W.; Liu, C. B.; Deng, Y. All-inorganic ultrathin high-sensitivity transparent temperature sensor based on a Mn–Co–Ni–O nanofilm. *Microsyst. Nanoeng.* **2024**, *10*, 70.

[7] Li, J. Y.; Ding, Q. L.; Wang, H.; Wu, Z. X.; Gui, X. C.; Li, C. W.; Hu, N.; Tao, K.; Wu, J. Engineering smart composite hydrogels for wearable disease monitoring. *Nano-Micro Lett.* **2023**, *15*, 105.

[8] Yao, P. Q.; Bao, Q. W.; Yao, Y.; Xiao, M.; Xu, Z. Y.; Yang, J. H.; Liu, W. G. Environmentally stable, robust, adhesive, and conductive supramolecular deep eutectic gels as ultrasensitive flexible temperature sensor. *Adv. Mater.* **2023**, *35*, 2300114.

[9] Zhang, C.; Zhou, Y. S.; Han, H. J.; Zheng, H. X.; Xu, W. H.; Wang, Z. K. Dopamine-triggered hydrogels with high transparency, self-adhesion, and thermoresponse as skinlike sensors. *ACS Nano* **2021**, *15*, 1785–1794.

[10] Wang, F.; Chen, J. W.; Cui, X. H.; Liu, X. N.; Chang, X. H.; Zhu, Y. T. Wearable ionogel-based fibers for strain sensors with ultrawide linear response and temperature sensors insensitive to strain. *ACS Appl. Mater. Interfaces* **2022**, *14*, 30268–30278.

[11] Yin, F. F.; Guo, Y. J.; Li, H.; Yue, W. J.; Zhang, C. W.; Chen, D.; Geng, W.; Li, Y.; Gao, S.; Shen, G. Z. A waterproof and breathable cotton/rGO/CNT composite for constructing a layer-by-layer structured multifunctional flexible sensor. *Nano Res.* **2022**, *15*, 9341–9351.

[12] Zhu, G. X.; Wang, F.; Chen, L. R.; Wang, C. B.; Xu, Y. Q.; Chen, J. W.; Chang, X. H.; Zhu, Y. T. Highly flexible TPU/SWCNTs composite-based temperature sensors with linear negative temperature coefficient effect and photo-thermal effect. *Compos. Sci. Technol.* **2022**, *217*, 109133.

[13] Qu, X. Y.; Sun, H. J.; Kan, X. L.; Lei, B.; Shao, J. J.; Wang, Q.; Wang, W. J.; Ni, Z. H.; Dong, X. C. Temperature-sensitive and solvent-resistance hydrogel sensor for ambulatory signal acquisition in "moist/hot environment". *Nano Res.* **2023**, *16*, 10348–10357.

[14] Zhao, H. F.; Ruan, L. G.; Wang, Z. H.; Shu, M. R.; Lyu, C.; Lakshan, B. R.; Ishara, D.; Wu, C. S.; Ding, W. B. Flexible nanogenerators for intelligent robotics: Design, manufacturing, and applications. *Int. J. Extrem. Manuf.* **2025**, *7*, 022012.

[15] Chen, X.; Zhou, J. C.; Huang, J. R.; Liu, J. H.; Nie, L. Y.; Zhu, Y. T. A neuromorphic multifunctional sensing fiber for deep learning enhanced wearable human-machine interaction. *Adv. Funct. Mater.* **2026**, *36*, e24652.

[16] Huang, J. R.; Liu, J. H.; Zhang, G. Y.; Nie, L. Y.; Xiong, Y.; Zhu, Y. T.; Wang, Z. L.; Sun, Q. J. Flexible sensor arrays with high-resolution and high-density. *Nano Energy* **2026**, *150*, 111748.

[17] Liu, H. D.; Du, C. F.; Liao, L. L.; Zhang, H. J.; Zhou, H. Q.; Zhou, W. C.; Ren, T. N.; Sun, Z. C.; Lu, Y. F.; Nie, Z. T. et al. Approaching intrinsic dynamics of MXenes hybrid hydrogel for 3D printed multimodal intelligent devices with ultrahigh superelasticity and temperature sensitivity. *Nat. Commun.* **2022**, *13*, 3420.

[18] Rao, J. H.; Chen, Z. T.; Zhao, D. N.; Ma, R.; Yi, W. Y.; Zhang, C. X.; Liu, D.; Chen, X.; Yang, Y. H.; Wang, X. F. et al. Tactile electronic skin to simultaneously detect and distinguish between temperature and pressure based on a triboelectric nanogenerator. *Nano Energy* **2020**, *75*, 105073.

[19] Zhang, X. J.; Chen, J. X.; Zheng, Z. H.; Tang, S. S.; Cheng, B.; Zhang, Z. W.; Ma, R.; Chen, Z. T.; Zhuo, J. T.; Cao, L. Y. et al. Flexible temperature sensor with high reproducibility and wireless closed-loop system for decoupled multimodal health monitoring and personalized thermoregulation. *Adv. Mater.* **2024**, *36*, 2407859.

[20] Chen, J. H.; Zhang, L.; Tu, Y. Y.; Zhang, Q.; Peng, F.; Zeng, W.; Zhang, M. Q.; Tao, X. M. Wearable self-powered human motion sensors based on highly stretchable quasi-solid state hydrogel. *Nano Energy* **2021**, *88*, 106272.

[21] Du, C. Y.; Hu, Y.; Xiao, X.; Manshaii, F.; Liang, L. R.; Chen, J.; Chen, G. M. High-reliability thermoreceptors with minimal temporal and spatial variations through photo-induced patterning thermoelectrics. *Nano-Micro Lett.* **2025**, *17*, 307.

[22] Lee, J. H.; Lee, K. Y.; Gupta, M. K.; Kim, T. Y.; Lee, D. Y.; Oh, J.; Ryu, C.; Yoo, W. J.; Kang, C. Y.; Yoon, S. J. et al. Highly stretchable piezoelectric-pyroelectric hybrid nanogenerator. *Adv. Mater.* **2014**, *26*, 765–769.

[23] Xue, H.; Yang, Q.; Wang, D. Y.; Luo, W. J.; Wang, W. Q.; Lin, M. S.; Liang, D. L.; Luo, Q. M. A wearable pyroelectric nanogenerator and self-powered breathing sensor. *Nano Energy* **2017**, *38*, 147–154.

[24] Qin, J.; Yin, L. J.; Hao, Y. N.; Zhong, S. L.; Zhang, D. L.; Bi, K.; Zhang, Y. X.; Zhao, Y.; Dang, Z. M. Flexible and stretchable capacitive sensors with different microstructures. *Adv. Mater.* **2021**, *33*, 2008267.

[25] You, I.; Mackanic, D. G.; Matsuhisa, N.; Kang, J.; Kwon, J.; Beker, L.; Mun, J.; Suh, W.; Kim, T. Y.; Tok, J. B. H. et al. Artificial multimodal receptors based on ion relaxation dynamics. *Science* **2020**, *370*, 961–965.

[26] Choi, H.; Jeong, U. Purposive design of stretchable composite electrodes for strain-negative, strain-neutral, and strain-positive ionic sensors. *Adv. Mater.* **2023**, *35*, 2306795.

[27] He, C. Y.; Wu, L.; Gu, G. Q.; Wei, L.; Yang, C. L.; Chen, M. An ionic assisted enhancement strategy enabled high performance flexible pressure-temperature dual sensor. *Nano Lett.* **2024**, *24*, 7040–7047.
[28] Hu, R. H.; Liu, P.; Zhu, W.; Guo, X.; Liu, Z.; Jin, Z. X.; Yang, R. H.; Han, J. W.; Tian, H. L.; Ma, Y. M. et al. Design, fabrication, and wearable medical application of a high-resolution flexible capacitive temperature sensor based on the thermotropic phase transition composites of PEO/PVDF-HFP/H_3PO_4. *Adv. Funct. Mater.* **2025**, *35*, 2417205.
[29] Ota, H.; Chen, K.; Lin, Y. J.; Kiriya, D.; Shiraki, H.; Yu, Z. B.; Ha, T. J.; Javey, A. Highly deformable liquid-state heterojunction sensors. *Nat. Commun.* **2014**, *5*, 5032.
[30] Prakash, K.; Sathian, S. P. Temperature-dependent differential capacitance of an ionic liquid-graphene-based supercapacitor. *Phys. Chem. Chem. Phys.* **2024**, *26*, 4657–4667.
[31] Chen, M.; Goodwin, Z. A. H.; Feng, G.; Kornyshev, A. A. On the temperature dependence of the double layer capacitance of ionic liquids. *J. Electroanal. Chem.* **2018**, *819*, 347–358.
[32] Lockett, V.; Sedev, R.; Ralston, J.; Horne, M.; Rodopoulos, T. Differential capacitance of the electrical double layer in imidazolium-based ionic liquids: Influence of potential, cation size, and temperature. *J. Phys. Chem. C* **2008**, *112*, 7486–7495.
[33] Hu, T.; Wang, J.; Zhang, H.; Li, Z.; Hu, M.; Wang, X. Vibrational properties of Ti_3C_2 and $Ti_3C_2T_2$ (T = O, F, OH) monosheets by first-principles calculations: A comparative study. *Phys. Chem. Chem. Phys.* **2015**, *17*, 9997–10003.
[34] Jiang, J. L.; Wen, D.; Zhao, W. C.; Zhao, L. Radiation-induced surface modification of MXene with ionic liquid to improve electrochemical properties and chemical stability. *Langmuir* **2023**, *39*, 13890–13896.
[35] Kiefer, J.; Fries, J.; Leipertz, A. Experimental vibrational study of imidazolium-based ionic liquids: Raman and infrared spectra of 1-ethyl-3-methylimidazolium bis(trifluoromethylsulfonyl)imide and 1-ethyl-3-methylimidazolium ethylsulfate. *Appl. Spectrosc.* **2007**, *61*, 1306–1311.
[36] Lu, Z. Q.; Jia, F. F.; Zhuo, L. H.; Ning, D. D.; Gao, K.; Xie, F. Microporous MXene/Aramid nanofibers hybrid aerogel with reversible compression and efficient EMI shielding performance. *Compos. B: Eng.* **2021**, *217*, 108853.
[37] Zhang, J. Q.; Zhou, X. J.; Wang, H. B.; Li, S. C.; Xi, H.; Zhong, P.; Wang, Z. N.; Liu, J. L.; Wu, H. J. Ionic liquid-armored MXene aerogels: Wrinkle engineering for promoting electromagnetic wave absorption. *Carbon* **2025**, *244*, 120723.
[38] Chang, Y.; Wang, L.; Li, R. Y.; Zhang, Z. C.; Wang, Q.; Yang, J. L.; Guo, C. F.; Pan, T. R. First decade of interfacial iontronic sensing: From droplet sensors to artificial skins. *Adv. Mater.* **2021**, *33*, 2003464.
[39] Wessendorf, A. M.; Newman, D. J. Dynamic understanding of human-skin movement and strain-field analysis. *IEEE Trans. Biomed. Eng.* **2012**, *59*, 3432–3438.
[40] Zhang, Q. T.; Tang, S. Y. Rethinking the need for ultra-high stretchability in stretchable electronics. *Health Nanotechnol.* **2025**, *1*, 10.
[41] Walters, T. J.; Blick, D. W.; Johnson, L. R.; Adair, E. R.; Foster, K. R. Heating and pain sensation produced in human skin by millimeter waves: Comparison to a simple thermal model. *Health Phys.* **2000**, *78*, 259–267.
[42] Dugbartey, G. J.; McFarlane, L.; Ortas, T. S.; Major, S.; Haig, A.; Sener, A. Augmented wound-healing effect of sodium thiosulfate-infused cosmetic creams in frostbite. *Pharmaceutics* **2025**, *17*, 1610.